Journal of
Materials Chemistry A

ROYAL SOCIETY
OF CHEMISTRY

PAPER

View Article Online
View Journal | View Issue

Cite this: *J. Mater. Chem. A*, 2025, **13**, 24151

Stable and efficient organic solar cells featuring an ultra-thin and transparent solution-deposited MoO_3 hole extraction layer†

Wisnu Tantyo Hadmojo, *[ab] Hendrik Faber, [a] Julien Gorenflot,[a]
Ryanda Enggar Anugrah Ardhi, [a] Zhaoheng Ling, [a] Qiao He,[c] Sarah Fearn,[c]
Ayman Rezk,[b] Muntaser Almansoori, [d] Ammar Nayfeh, [b] Martin Heeney, [a]
Frédéric Laquai [a] and Thomas D. Anthopoulos *[ae]

The development of non-fullerene acceptor (NFA) based organic solar cells (OSCs) featuring self-assembled monolayers (SAMs) as the transparent hole extraction layers (HELs) has led to power conversion efficiency (PCE) values of over 20%. Unfortunately, SAM-based OSCs exhibit limited operational stability due to their sensitivity to elevated temperature and light stress. Here, we tackled this issue by developing NFA-based OSCs using ultrathin solution-processed molybdenum oxide (s-MoO_x) as the HEL. Devices featuring s-MoO_x exhibited superior stability while retaining a similar PCE to 2PACz-based cells (∼17.3%). The time required for the initial PCE of cells based on ITO/2PACz and the ITO/s-MoO_x to degrade by 20% (T_{80}) under continuous thermal stress at 85 °C in nitrogen was 15 and 600 h, respectively, highlighting the crucial role of HELs in operational stability. Analysis using time-of-flight secondary ion mass spectroscopy (ToF-SIMS) reveals that in cells with ITO/SAM, the diffusion of electrode elements and 2PACz and chemical interactions with the NFA are responsible for the performance degradation observed. Replacing 2PACz with s-MoO_x significantly suppressed the diffusion of ITO and prevented its interaction with the organic semiconductor. Our work revealed the crucial roles of HELs and could help in developing efficient and more stable OSCs.

Received 28th April 2025
Accepted 19th June 2025

DOI: 10.1039/d5ta03360h

rsc.li/materials-a

Introduction

The advent of non-fullerene acceptor (NFA) materials has enabled the development of organic solar cells (OSCs) with a power conversion efficiency (PCE) of over 20% in single[1–4] and multi-junction[5,6] solar cells. To advance their performance further, numerous methods have been developed and include a combination of new active materials,[7] additives,[8] interlayers,[9] and innovative device processing protocols.[10] Besides PCE, recent developments in OSCs have also shown encouraging improvement in their long-term stability.[11] Improvements in PCE and OSC stability are typically achieved through the meticulous development of donor and acceptor organic-based absorbers. Utilising a deep energy level donor to prevent oxidation,[12] avoiding the use of labile H atoms,[13] and vulnerable chemical bonds in the side chains[14] have been explored to minimise photodegradation and enhance the stability of polymer-based donor materials. Meanwhile, the photostability of NFA-based materials can be improved by avoiding susceptible vinyl groups[15] and using steric interactions to resist isomerisation.[16] However, the degradation of OSCs is significantly more complex, as it may involve numerous combinations of active materials and interlayers that could contribute to degradation, holding back the progress towards more stable OSCs.

Charge extraction layers are also an important part of OSCs that often determine the overall efficiency[17] and their long-term stability.[18–20] The front-type extraction/interlayer located between the transparent electrode (ITO) and BHJ is especially important. Front-type extraction/interlayer should be transparent and sufficiently robust to withstand the deposition of the next layer during fabrication and intense light during operation. The widely used organic p-type interlayer PEDOT:PSS, has poor thermal- and photo-stability due to the acidity and decreased conductivity,[21] while n-type electron transport layers (ETLs), such as PDI-based and PFN-Br, decompose or aggregate

---

[a] Physical Sciences and Engineering Division (PSE), King Abdullah University of Science and Technology (KAUST), Thuwal, 23955-6900, Kingdom of Saudi Arabia. E-mail: wisnu.hadmojo@ku.ac.ae

[b] Department of Electrical Engineering, Khalifa University, United Arab Emirates

[c] Department of Chemistry and Centre for Processable Electronics, Imperial College London, London W12 0BZ, UK

[d] Department of Mechanical & Nuclear Engineering, Khalifa University, United Arab Emirates

[e] Henry Royce Institute and Photon Science Institute, Department of Electrical and Electronic Engineering, The University of Manchester, Oxford Road, Manchester M13 9PL, UK. E-mail: thomas.anthopoulos@manchester.ac.uk

† Electronic supplementary information (ESI) available. See DOI: https://doi.org/10.1039/d5ta03360h

under high thermal stress.[22,23] Moreover, metal oxide-based interlayers, such as zinc oxide (ZnO), have inherent stability issues owing to their photocatalytic behaviour under intense light exposure that decomposes non-fullerene acceptors.[24] Despite being reported to have good stability, molybdenum oxide, MoO_x, is rarely utilised as a front hole transport layer (HTL) because of its parasitic absorbance and high-temperature processing under vacuum.[25,26]

Recently, ultrathin hole extraction layers (HELs) featuring self-assembled monolayers (SAMs) have shown excellent performance, owing to their adjustable energy levels and transparency, achieving a PCE of >19%.[27–30] SAMs can be mixed with other components to further enhance the performance.[31,32] Cells featuring a bilayer of metal oxide interlayers and SAMs were adopted to achieve better coverage of SAMs.[33,34] Furthermore, SAMs have been reported to be suitable for large-area solution processing OSCs, achieving a PCE of nearly 18% for 1 cm^2 devices, an important progress towards commercialization.[35] Finally, state-of-the-art PCE values of nearly 21% and 27% in OSCs[4] and perovskite solar cells,[36] respectively, feature SAMs as HELs. However, despite their excellent PCE, SAM based HELs were reported to have issues related to their long-term stability under illumination due to the photochemical degradation of SAMs.[37] Moreover, there is a lack of reports discussing the cause of the instability of SAM-based HELs under thermal stress.

Previously, we used a combination of thermally evaporated MoO_x (e-MoO_x) and 2PACz SAM (e-MoO_x/SAM) as the HEL and PM6:L8-BO as the active layer to demonstrate stable OSCs.[38] However, despite the encouraging preliminary results, using ITO/e-MoO_x/2PACz results in a lower PCE than cells with ITO/2PACz owing to the parasitic absorption of e-MoO_x. Moreover, the degradation mechanism of ultrathin-based 2PACz is not well understood. Herein, we developed an alternative HEL using solution-processed MoO_x (s-MoO_x).[39] Compared with the initial reference, s-MoO_x was dissolved in water without mixing with HCl to prevent potential damage to the ITO. As the HEL, s-MoO_x features nearly identical transparency, thickness, and energy levels to 2PACz. Cells featuring ITO/s-MoO_x electrodes achieved a PCE of 17.3%, almost the same as cells based on ITO/2PACz. The stability of ITO/s-MoO_x-based cells, assessed by the time required for their initial PCE to reach 80% of its initial value (T_{80}) under thermal/light stress and maximum power tracking, is much higher (600 and 37 h, respectively) than that of ITO/2PACz-based cells (15 and 1.2 h, respectively). Analysis of the cells before and after stressing using mass spectrometry suggested that the diffusion of ITO and 2PACz and their interaction with active materials in the bulk heterojunction caused changes in the L8-BO, which most likely underpins the drop in PCE. The findings could help improve the operational stability of next-generation OSCs based on ultra-thin HELs.

Results and discussion

The molecular structures of 2PACz and the donor/acceptor active materials, PM6/L8-BO, are shown in Fig. 1a. 2PACz and s-MoO_x were deposited on ITO by spin coating at 5000 rpm, followed by thermal annealing at 80 °C for 1 min (2PACz) or 150

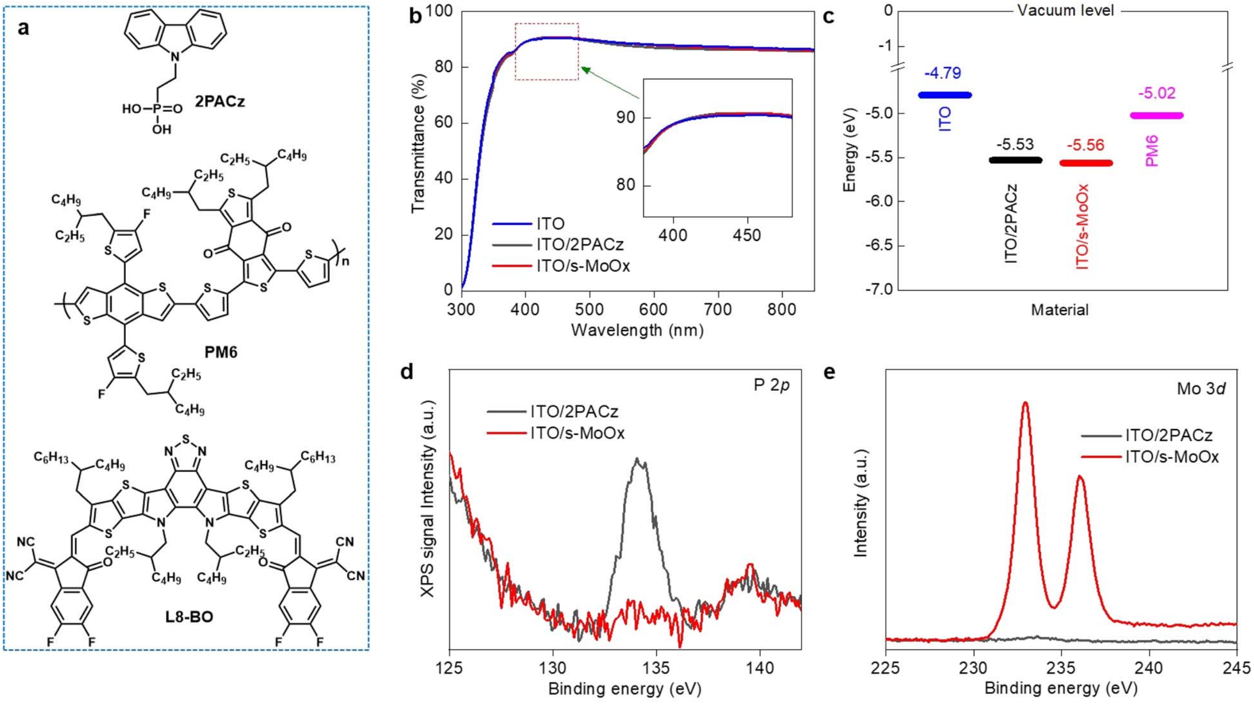

Fig. 1 (a) Molecular structure of 2PACz, PM6, and L8-BO. (b) Transmission spectra of various HELs. The inset shows the zoom in of transmittance between 300 and 450 nm. The transmittance of ITO, ITO/2PACz and ITO/s-MoO_x was nearly identical. (c) IE of HELs relative to PM6, measured by PESA. (d) XPS spectra of the P 2p signal of various HELs. (e) XPS spectra of the Mo 3d signal of various HELs.

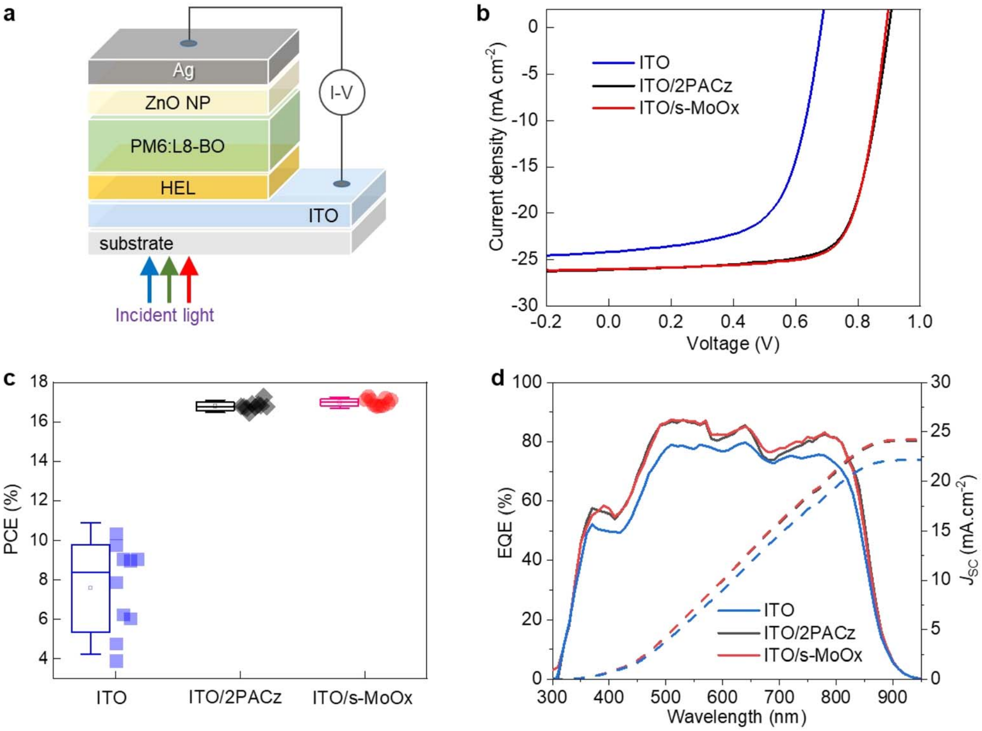

Fig. 2 (a) Device configuration and (b) J–V curves. (c) Statistics based on 10 cells, and (d) EQE of OSCs based on PM6:L8-BO as active materials and ITO, ITO/2PACz, and ITO/s-MoO$_x$ as HELs.

°C for 30 min (s-MoO$_x$), respectively. The optical transmittance spectra of ITO, ITO/2PACz, and ITO/s-MoO$_x$ are shown in Fig. 1b. There is almost identical transmittance between ITO, ITO/2PACz, and ITO/s-MoO$_x$ because 2PACz and s-MoO$_x$ are very thin and transparent. Because of its ultra-thin and transparent properties, measuring the thickness of 2PACz and s-MoO$_x$ accurately is challenging. The thickness of 2PACz was approximately ∼3 nm,[37] whereas that of s-MoO$_x$ was approximately <5 nm, measured using ellipsometry. Photoelectron spectroscopy in air (PESA) was used to measure the ionisation energy (IE) of the various HELs relative to PM6 (Fig. S1†). The IE levels of ITO, ITO/2PACz, ITO/s-MoO$_x$, and PM6 were −4.79 eV, −5.53 eV, −5.56 eV, and −5.02 eV, respectively, and are shown in Fig. 1c. ITO/2PACz and ITO/s-MoO$_x$ exhibit nearly identical deep IE, making them suitable for electron blocking while allowing holes to transfer from PM6 to the ITO electrode.

X-ray photoelectron spectroscopy (XPS) was used to detect the presence of an ultrathin HEL on top of the ITO. The presence of 2PACz and s-MoO$_x$ was determined by measuring the P and Mo signals, respectively. The measured positions of the P 2p signal for ITO/2PACz[40] and the Mo 3d signal for s-MoO$_x$[41] are consistent with the literature. The P 2p signal was detected on ITO/2PACz with a binding energy of 134 eV, whereas the Mo 3d doublet signal was detected on ITO/s-MoO$_x$ with two peaks at 233 eV and 236 eV, as shown in Fig. 1d and e, respectively. Moreover, XPS results suggest that the chemical composition of s-MoO$_x$ is close to its stoichiometric composition of MoO$_3$.[42]

The surface topography of ITO after the deposition of the various HEL materials was measured using atomic force microscopy (AFM) (Fig. S2†). ITO, ITO/2PACz and ITO/s-MoO$_x$ exhibited nearly identical features dominated by the rough underlying ITO electrode. The ITO/s-MoO$_x$ yielded a slightly lower roughness (2.96 nm) than ITO (3.30 nm) and ITO/2PACz (3.25 nm), suggesting that the presence of 2PACz and s-MoO$_x$ did not significantly alter the surface morphology of ITO.

Next, we fabricated solar cells with a p–i–n (conventional) architecture to assess the effects of different HELs on the performance of OSCs (Fig. 2a). PM6 and L8-BO were used as the active materials, whereas ZnO nanoparticles (NPs) were used as the ETL because of the excellent energetics and operational stability.[38] The J–V curves and EQE of the corresponding cells are shown in Fig. 2b–d and S3,† while a summary of the device parameters is given in Table 1. Devices featuring 2PACz and s-MoO$_x$ as the HEL exhibited nearly identical PCE (17.26% and 17.27%, respectively). Moreover, other important parameters, such as V_{OC}, J_{SC}, FF, EQE, and statistics, were nearly identical because of their very similar optoelectronic properties. Interestingly, cells without any HEL (ITO only) exhibited significantly lower V_{OC}, FF, and PCE (9.70%). Despite having the same surface and optical properties, severe recombination at the interface caused by misalignment of the energy level decreases the J_{SC} and EQE of cells without any HEL, compared to cells featuring 2PACz and s-MoO$_x$, as shown in Fig. 2d.

The recombination properties of the different HELs were studied using transient photovoltage (TPV),[43] as shown in Fig. S4a.† The superior performance of the device based on ITO/2PACz and ITO/s-MoO$_x$ compared to bare ITO only was reflected by their superior charge carrier lifetime, which was

Table 1 Best solar cell parameters measured for PM6:L8-BO OSCs featuring ITO, ITO/2PACz, and ITO/s-MoO$_x$ as HELs. The statistics were derived from measurements performed on 10 devices

HEL	PCE (%)	V_{OC} (V)	J_{SC} (mA cm^{-2})	$J_{SC,EQE}$ (mA cm^{-2})	FF (%)
No HEL (ITO only)	10.31 (7.56 ± 2.11)	0.68 (0.54 ± 0.11)	24.12 (24.55 ± 0.69)	22.40	62.62 (55.75 ± 5.78)
2PACz	17.26 (16.79 ± 0.19)	0.90 (0.90 ± 0.01)	26.16 (25.69 ± 0.35)	24.38	73.57 (72.32 ± 0.51)
s-MoO$_x$	17.27 (16.98 ± 0.18)	0.90 (0.90 ± 0.01)	26.07 (25.90 ± 0.23)	24.49	73.64 (72.97 ± 0.72)

determined to be 7.54 μs, 7.21 μs, and 3.83 μs, respectively. Furthermore, the charge collection efficiency at the maximum power point (MPP) (P_{MPP}) and under short-circuit conditions (P_{SC}) was calculated by analysing the V_{eff} *vs.* J_{ph} of the cells (Fig. S4b†). Devices based on ITO/2PACz and ITO/s-MoO$_x$ exhibited nearly identical and enhanced P_{MPP} and P_{SC} compared to ITO. Devices based on ITO/2PACz and ITO/s-MoO$_x$ exhibit nearly identical photovoltaic parameters. These similarities are attributed to the nearly identical charge transfer characteristics, optical transparencies, IE, and surface topographies of the two HEL systems. Meanwhile, devices without any HEL (bare ITO) exhibit significantly lower V_{OC}, J_{SC}, FF and charge transfer properties due to mismatched IE and severe charge carrier recombination.[44] Moreover, and despite their ultrathin nature, ITO/2PACz and ITO/s-MoO$_x$ exhibit significantly lower device parameter deviation than cells based on bare ITO, indicating high reproducibility (Fig. 2c and S3†).

The thermal stability of different HELs was also assessed by placing the cells in a nitrogen atmosphere in the dark at 85 °C and monitoring the evolution of the device parameters over 1000 hours (Fig. 3). Over this period, devices based on bare ITO and ITO/2PACz show severe degradation, with a T_{80} of only 8 and 15 h, respectively. Rapid deterioration in V_{OC} and FF is observed for ITO/2PACz, while bare ITO cells suffer additional deterioration in their J_{SC}. These trends are similar to what we observed previously, suggesting that degradation is related to the interaction between the ITO electrode and the BHJ.[38] When ITO/s-MoO$_x$ was used, the ensuing cells showed significantly higher thermal stability with a T_{80} of 600 h while retaining ~70% of their initial PCE after 1000 h.

To elucidate the origin of degradation in cells featuring the different HELs, we analysed the surface topographies of ITO, ITO/2PACz, and ITO/s-MoO$_x$ electrodes after thermal annealing at 85 °C for 200 h using AFM (Fig. S5†). No major changes in the surface morphologies are observed, with all three electrodes retaining their initial surface characteristics (Fig. S2†). Next, we perform AFM imaging on ITO/2PACz/PM6:L8-BO and ITO/s-MoO$_x$/PM6:L8-BO samples before and after thermal annealing (Fig. S6†). Fresh devices based on ITO/2PACz/L8-BO exhibit higher surface roughness (1.39 nm) than ITO/s-MoO$_x$/BHJ (1.11 nm). The surface roughness increases slightly upon thermal annealing, and both devices appear more fibril-like. The well intertwined nano-scale fibrillar morphology has been reported to allow efficient exciton dissociation and charge transport.[45–47]

The effect of thermal stress on the charge transport in cells with different HELs was examined using the space charge limited current (SCLC) method. The obtained data are shown in Fig. 4a–c, while Table S1† summarises the extracted parameters.

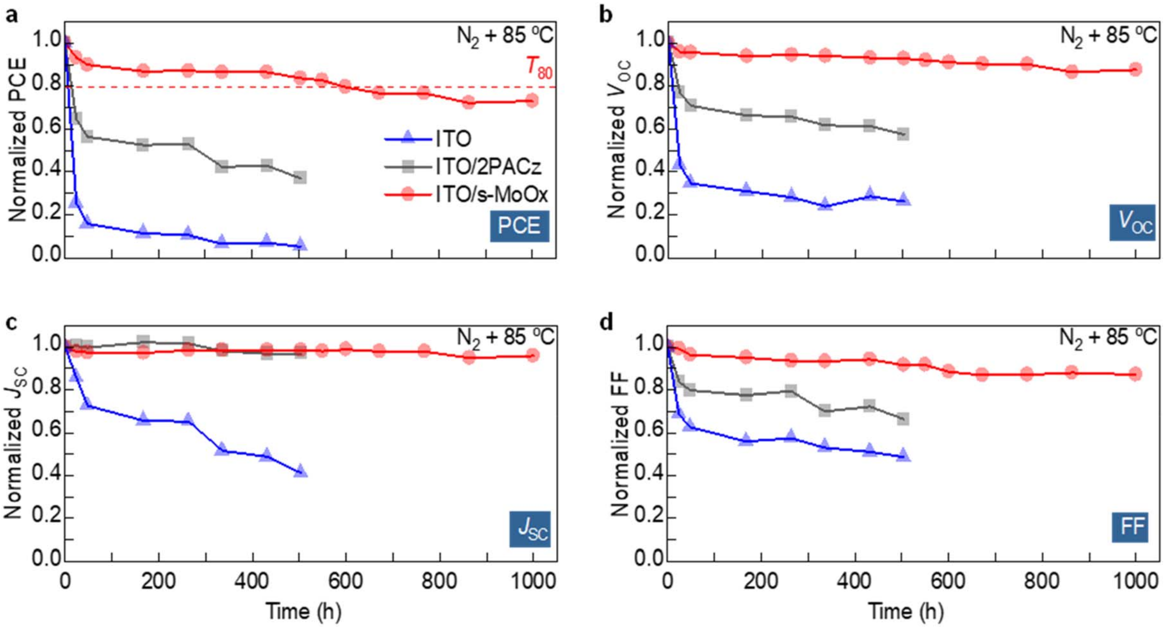

Fig. 3 Evolution of cells parameters including (a) PCE, (b) V_{OC}, (c) J_{SC}, and (d) FF featuring PM6:L8-BO as active materials and ITO, ITO/2PACz, and ITO/s-MoO$_x$ as HELs. Cells were stored under a dark and N$_2$ atmosphere while being continuously annealed at 85 °C for 1000 h.

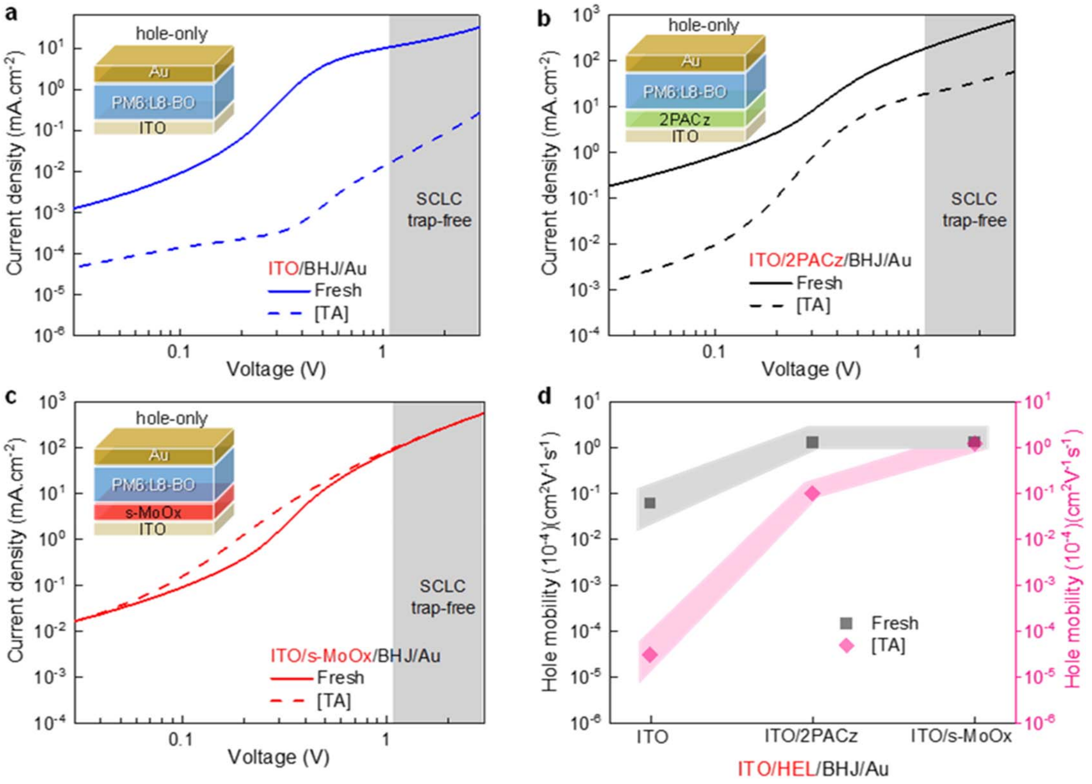

Fig. 4 (a)–(c) Hole-only SCLC measurements of PM6:L8-BO cells featuring ITO, ITO/2PACz, and ITO/s-MoO$_x$ HELs before (solid lines) and after thermal annealing ([TA], dashed lines) at 85 °C for 200 h. (d) The calculated hole mobility featuring different HELs before (black dots, left-Y) and after (red dots, right-Y) thermal annealing.

Fresh devices featuring bare ITO exhibit low hole mobility (0.06 $\times$ 10^{-4} cm^2 V^{-1} s^{-1}), while cells based on ITO/2PACz and ITO/s-MoO$_x$ yield higher and nearly identical values of ~1.30 × 10–4 cm^2 V^{-1} s^{-1}. The evolution of hole mobility for fresh and thermally annealed cells based on different HELs is presented in Fig. 4d. After thermal annealing for 200 h, the hole mobility in cells with bare ITO and ITO/2PACz significantly dropped, while the hole mobility in devices featuring the ITO/s-MoO$_x$ remained largely unchanged. Moreover, we performed transient photocurrent (TPC) measurement to probe further the effect of thermally induced degradation (Fig. S7†). Fresh cells based on ITO/2PACz and ITO/s-MoO$_x$ showed fast rise and fall times. However, after annealing for 200 h, cells based on ITO/2PACz show significantly slower rise and fall traces, which indicates the formation of deep trap states,[48] whereas cells based on ITO/s-MoO$_x$ were only slightly affected.

We performed electrochemical impedance spectroscopy (EIS) (Fig. 5) to study each layer's contribution as a function of thermal annealing (Table 2). By fitting the data using the Nyquist plot and comparing it with the equivalent electrical circuit, the total resistance associated with the electrodes ($R_{\text{electrodes}}$), all interfaces ($R_{\text{interfaces}}$), and the BHJ film (R_{BHJ}) was calculated. After thermal annealing, $R_{\text{electrodes}}$ values of cells based on ITO/2PACz and ITO/s-MoO$_x$ have negligible change. This indicates that the electrical properties of electrodes (ITO and Ag) are relatively stable under thermal stress. Interestingly, thermal annealing increases R_{BHJ} of ITO/2PACz from 54.7 to 86.5 Ω cm^2, whereas that of ITO/s-MoO$_x$ increases from 40.9 to 51.0 Ω cm^2. This implies that the deterioration of BHJ based on ITO/2PACz is more prominent than in cells featuring ITO/s-MoO$_x$. Finally, the $R_{\text{interfaces}}$ of cells based on ITO/2PACz increased 75-fold from 29 to 2187 Ω cm^2, whereas that of ITO/s-MoO$_x$ increased two-fold from 23.5 to 45.5 Ω cm^2. This suggests that the cell performance degradation originates predominantly from the interfaces in the device.

The capacitor (C) accounts for the dielectric behaviour of the entire solar cell.[49] The constant phase element (CPE), which consists of pseudo-capacitance (CPE-T) and an inhomogeneous capacitive constant (CPE-P), describes the capacitive properties of a non-ideal capacitor and is used to define the average lifetime (τ) of charge carriers at the BHJ and interfaces.[50,51] The $\tau_{(\text{BHJ})}$ and $\tau_{(\text{interfaces})}$ of cells based on ITO/2PACz after thermal annealing decrease by nearly half of their initial value from 35.7 to 20.8 μs and 15.6 to 7.2 μs, respectively. Meanwhile, the $\tau_{(\text{BHJ})}$ and $\tau_{(\text{interfaces})}$ of cells based on ITO/s-MoO$_x$ after thermal annealing only slightly decreased from 38.5 to 30.8 μs and 25.8 to 22.8 μs. Cells without a HEL (*i.e.* bare ITO) were omitted from TPC and EIS measurements as the devices were not functioning after 200 h of continuous thermal annealing. These results suggest that interfaces between ITO, HEL, and BHJ are the main cause of thermally induced degradation and that utilising s-MoO$_x$ yields cells with remarkably improved resistance to thermal stress.

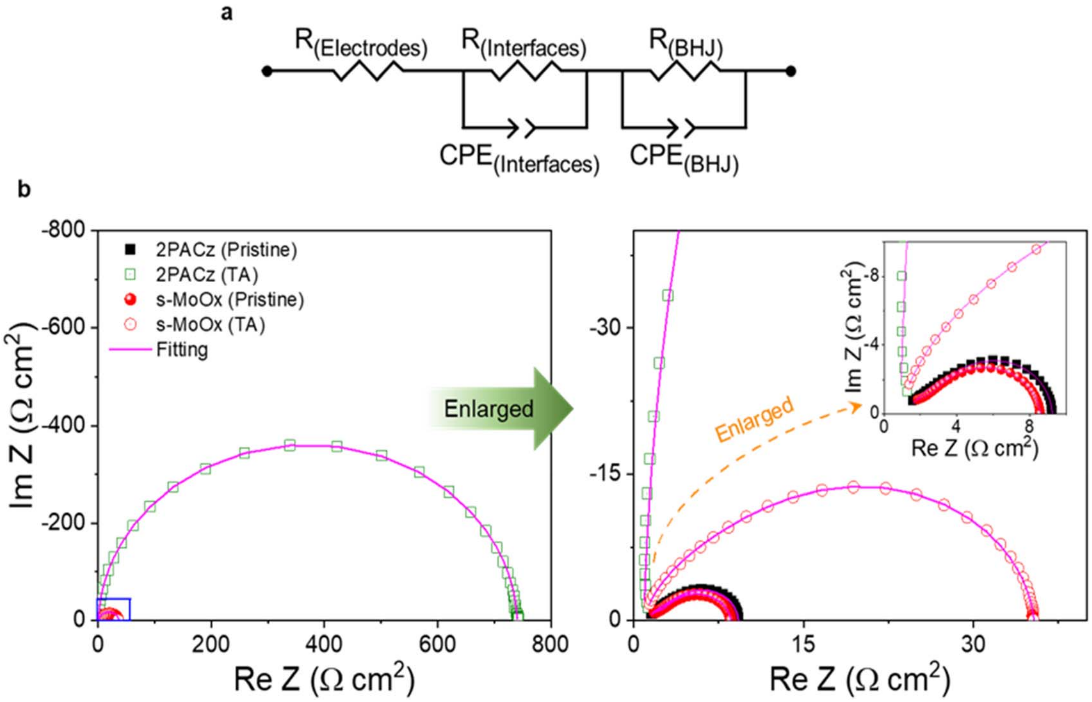

Fig. 5 (a) The equivalent circuit of OSCs to simulate the EIS measurements. (b) EIS Nyquist plot of fresh and thermally annealed [TA] at 85 °C for 200 h of PM6:L8-BO with cell architectures of ITO/2PACz/BHJ/ZnO/Ag and ITO/s-MoO_x/BHJ/ZnO/Ag. The area inside the blue rectangle of the left image was enlarged and shown in the right image.

The origin of thermally induced degradation on the cell performance was further investigated using time-of-flight secondary ion mass spectrometry (ToF-SIMS). The molecular depth profiles and illustrations of half-full devices consisting of ITO/PM6:L8-BO, ITO/2PACz/PM6:L8-BO, and ITO/s-MoO_x/PM6:L8-BO before and after 200 h of thermal annealing are presented in Fig. 6. Molecular clusters corresponding to In_2O_3, PO_3, MoO_3, and IC-2F were tracked, resulting exclusively from ITO, 2PACz, s-MoO_x, and L8-BO, respectively. We note that F is associated with both PM6 and L8-BO as it is present in both materials. Fresh ITO/PM6:L8-BO featured a not-sharp slope of InO_2, suggesting the presence of a diffused interface between the ITO and the BHJ. After thermal annealing, the intensity of IC-2F was severely weakened across the entire film, suggesting major changes in the L8-BO. Furthermore, the intensity of In_2O_3 up to the interface between PM6:L8-BO (under a scattering time of up to 500 s) also decreased, which indicates a possible change in ITO due to interaction with L8-BO. Fresh ITO/2PACz/PM6:L8-BO showed a sharp slope for both PO_3 and In_2O_3 signals indicating no diffusion into PM6:L8-BO. However, after thermal annealing, signs of 2PACz and ITO diffusion into PM6:L8-BO exist. Specifically, the PO_3 and In_2O_3 signals showed that the interface was no longer sharp following prolonged thermal annealing. The intensity of In_2O_3 up to the interface between the ITO, 2PACz, and PM6-BHJ also decreased. In addition, the intensity of IC-2F was reduced across the entire film. Meanwhile, the fresh ITO/s-MoO_x/PM6:L8-BO showed no indication of ITO or s-MoO_x diffusion. After thermal annealing, there was a negligible change in all the elements with no signs of diffusion, with the intensity of IC-2F remaining similar, indicating no change to that of L8-BO. Furthermore, the intensity of In_2O_3 up to the interface between the ITO, s-MoO_x, and PM6:L8-BO did not change. In all devices, PM6 showed negligible changes after thermal annealing. These results suggest that the diffusion of ITO and 2PACz and the changes occurring in ITO and L8-BO related to the molecular cluster of 2F might cause cell degradation under thermal annealing. Unfortunately, at

Table 2 Summary of parameters extracted from EIS from Fig. 5. S1 refer to ITO/2PACz/BHJ/ZnO/Ag, and S2 refers to ITO/s-MoO_x/BHJ/ZnO NP/Ag. elec refers to electrodes, and int refers to interfaces

Structure	R_{elec} (Ω cm^2)	R_{int} (Ω cm^2)	R_{BHJ} (Ω cm^2)	CPE-T_{int} (nF cm^{-2})	CPE-P_{int}	CPE-T_{BHJ} (nF cm^{-2})	CPE-P_{BHJ}	$\tau_{(int)}$ (μs)	$\tau_{(BHJ)}$ (μs)
S1	12.2	29.0	54.7	537	0.95	44.0	0.98	15.6	35.7
[TA] S1	9.0	2187.0	86.5	3.3	0.77	4.1	0.95	7.2	20.8
S2	7.6	23.5	40.9	1100	0.99	84.0	0.99	25.8	38.5
[T2] S2	8.6	45.5	51.0	501	0.98	60.3	0.98	22.8	30.8

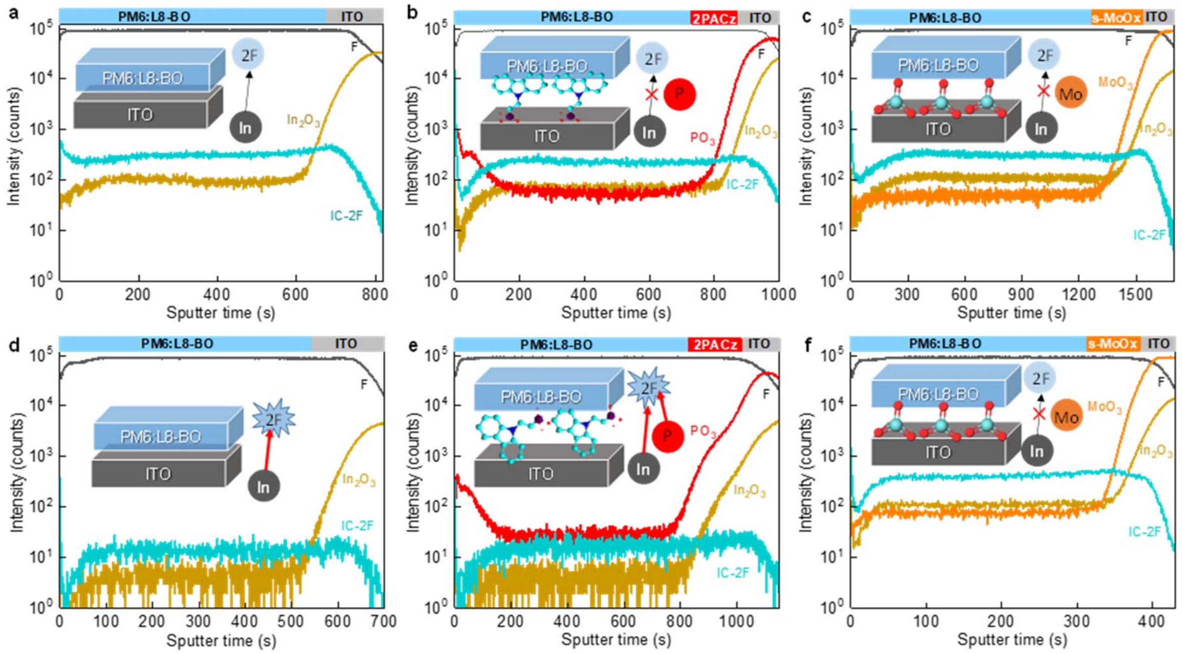

Fig. 6 Depth profile of fresh (a)–(c) and after thermal annealing at 85 °C for 200 h (d)–(f) of half-full cells based on ITO, ITO/2PACz, and ITO/s-MoO_x as the HEL and PM6:L8-BO as the BHJ measured by ToF-SIMS. Illustrations suggesting the diffusion of ITO, 2PACz, and the degradation of L8-BO are shown.

this stage we are unable to identify the nature of those chemical interactions.

Finally, the operational stability, which requires the cells to be exposed to continuous light illumination and bias voltage to maintain MPP conditions, was studied (Fig. S8†). OSCs without any HEL (bare ITO) exhibit worst stability and degrade almost instantly yielding $T_{80} = 0.07$ h. Cells based on ITO/2PACz yield an improved T_{80} of 1.2 h. To this end, it has been reported that 2PACz exhibits poor light stability, as the molecule decomposes and reacts with the photoactive materials under prolonged intense illumination.[38,44] Cells based on ITO/s-MoO_x show superior operational stability with a T_{80} of 37 h. Lastly, cells featuring PEDOT:PSS and e-MoO_x/2PACz were fabricated, and the J–V curves are shown in Fig. S9† with their operating characteristics summarized in Table S2.† Devices featuring PEDOT:PSS and e-MoO_x/2PACz as the HTL exhibited lower PCE of 16.65% and 16.42%, respectively, than those of 2PACz or s-MoO_x because of the lower J_{SC} and FF owing to the parasitic absorbance and slightly inferior charge extraction. The evolution of the solar cell parameters of the HTL featuring PEDOT:PSS and e-MoO_x/2PACz under thermal annealing is shown in Fig. S10.† Cells featuring PEDOT:PSS showed deterioration of V_{OC} and FF, suggesting recombination and a T_{80} of 390 h. Interestingly, the J_{SC} of the cells featuring PEDOT:PSS was enhanced and retained a high value after thermal annealing, suggesting different degradation mechanisms. Furthermore, the operational stability of cells featuring PEDOT:PSS achieved T_{80} of 3.8 h, as shown in Fig. S11.† Cells featuring ITO/PEDOT:PSS as the HTL showed superior thermal and operational stability compared to cells featuring ITO/2PACz and bare ITO but inferior to ITO/s-MoO_x. Meanwhile, cells featuring ITO/e-MoO_x/2PACz exhibited superior thermal stability with a T_{80} of 700 h, comparable to ITO/s-MoO_x, and higher compared to cells featuring ITO/2PACz, ITO/PEDOT:PSS, and bare ITO. The evolution of the parameters of the cells featuring ITO/e-MoO_x/2PACz under thermal stress is similar to that of ITO/s-MoO_x, suggesting that e-MoO_x also resists ITO and 2PACz diffusion to the active materials. Our findings underline the critical role of s-MoO_x as the front hole extraction interlayer and its ability to prevent degradation induced by interactions occurring between ITO and the BHJ components. Furthermore, compared to other metal oxide based HTLs, the ultrathin and transparent s-MoO_x can potentially be paired with various SAMs to adjust the energy level and avoid parasitic absorbance. A summary of OSCs featuring various SAMs as HELs is provided in Table S3.†

Conclusions

We reported OSCs based on an ultra-thin and transparent front-hole extraction layer and studied their performance and stability. Our study revealed that cells based on ITO/s-MoO_x have nearly identical performance to cells based on ITO/2PACz because their optical, morphological, energy level, and charge transfer properties are nearly identical. However, devices based on ITO/2PACz and without any HEL rapidly degrade under thermal annealing. Our findings suggest that the degradation was due to the diffusion of ITO and 2PACz, and changes occurring in L8-BO, related to the molecular cluster of 2F, leading to poor long-term stability. Replacing 2PACz with s-MoO_x prevented the diffusion of ITO and changes in L8-BO, considerably enhancing the long-term stability. Cells based on ITO/s-MoO_x also showed a higher PCE and long-term stability than those based on ITO/PEDOT:PSS. Our work reveals the mechanism behind the thermally induced degradation of OSCs based on ultra-thin HELs and efficient PCE (>17%) with long-term stability by utilizing s-MoO$_x$. Furthermore, ultrathin and transparent s-MoO$_x$ can be potentially paired with various SAMs to optimize the energy levels for the future development of solar cells.

Data availability

Data for this article, including *J–V*, EQE, and thermal stability are available at: **https://osf.io/57fvy/files/osfstorage/680f5c1231ef11bde7568c28**.

Author contributions

W. T. H. and T. D. A. conceived the study. W. T. H., Z. L., and R. E. A. A. designed and characterized the devices. H. F. assisted with the device's operational stability analysis. Q. H. and S. F. performed ToF-SIMS measurements and analysis. A. R. and M. A. performed ellipsometry and prepared illustrations under the supervision of A. N. W. T. H., J. G., and T. D. A. wrote the original draft. T. D. A. and F. L. supervised the project. All authors contributed to analysis, discussion, and manuscript preparation.

Conflicts of interest

There are no conflicts to declare.

Acknowledgements

This publication was supported by the King Abdullah University of Science and Technology (KAUST) office of Research Administration (ORA) under award No. OSR-CCF-3079 and OSR-2016-CRG5-3029.

Notes and references

1 Z. Chen, J. Ge, W. Song, X. Tong, H. Liu, X. Yu, J. Li, J. Shi, L. Xie, C. Han, Q. Liu and Z. Ge, *Adv. Mater.*, 2024, **36**, 2406690.

2 Z. Ling, J. Wu, J. P. Jurado, C. E. Petoukhoff, S. Y. Jeong, D. Naphade, M. Babics, X. Chang, H. Faber, S. Doukas, E. Lidorikis, M. I. Nugraha, M. He, M. Alqurashi, Y. Lin, X. Sun, H. Hu, H. Y. Woo, S. De Wolf, L. Tsetseris, F. Laquai, D. Yu, E. Wang and T. D. Anthopoulos, *Mater. Sci. Eng. R Rep.*, 2025, **163**, 100922.

3 L. Zhu, M. Zhang, G. Zhou, Z. Wang, W. Zhong, J. Zhuang, Z. Zhou, X. Gao, L. Kan, B. Hao, F. Han, R. Zeng, X. Xue, S. Xu, H. Jing, B. Xiao, H. Zhu, Y. Zhang and F. Liu, *Joule*, 2024, **8**, 3153–3168.

4 S. Xu, Y. Zhang, Y. Sun, P. Cheng, Z. Yao, N. Li, L. Ye, L. Zuo and K. Gao, *Nanomicro Lett.*, 2025, **17**, 37.

5 J. Wang, Z. Zheng, P. Bi, Z. Chen, Y. Wang, X. Liu, S. Zhang, X. Hao, M. Zhang, Y. Li and J. Hou, *Natl. Sci. Rev.*, 2023, **10**(6), nwad085.

6 Z. Zheng, J. Wang, P. Bi, J. Ren, Y. Wang, Y. Yang, X. Liu, S. Zhang and J. Hou, *Joule*, 2022, **6**, 171–184.

7 Z. Chen, J. Zhu, D. Yang, W. Song, J. Shi, J. Ge, Y. Guo, X. Tong, F. Chen and Z. Ge, *Energy Environ. Sci.*, 2023, **16**, 3119–3127.

8 Z. Ling, M. I. Nugraha, W. T. Hadmojo, Y. Lin, S. Y. Jeong, E. Yengel, H. Faber, H. Tang, F. Laquai, A.-H. Emwas, X. Chang, T. Maksudov, M. Gedda, H. Y. Woo, I. McCulloch, M. Heeney, L. Tsetseris and T. D. Anthopoulos, *ACS Energy Lett.*, 2023, **8**, 4104–4112.

9 Z. Wang, H. Wang, M. Du, X. Lai, F. He, Q. Guo, Q. Guo, A. Tang, X. Sun and E. Zhou, *Adv. Funct. Mater.*, 2024, **34**, 2313240.

10 S. Luo, C. Li, J. Zhang, X. Zou, H. Zhao, K. Ding, H. Huang, J. Song, J. Yi, H. Yu, K. S. Wong, G. Zhang, H. Ade, W. Ma, H. Hu, Y. Sun and H. Yan, *Nat. Commun.*, 2023, **14**, 6964.

11 J. Han, H. Xu, S. H. K. Paleti, A. Sharma and D. Baran, *Chem. Soc. Rev.*, 2024, **53**, 7426–7454.

12 I. V. Martynov, L. N. Inasaridze and P. A. Troshin, *ChemSusChem*, 2022, **15**, e202101336.

13 H. Hintz, H.-J. Egelhaaf, L. Lüer, J. Hauch, H. Peisert and T. Chassé, *Chem. Mater.*, 2011, **23**, 145–154.

14 A. Tournebize, I. Fraga Domínguez, G. E. Morse, C. Taviot-Guého, A. Rivaton, H. Peisert and T. Chassé, *Polym. Degrad. Stab.*, 2017, **146**, 155–160.

15 J. Luke, E. M. Speller, A. Wadsworth, M. F. Wyatt, S. Dimitrov, H. K. H. Lee, Z. Li, W. C. Tsoi, I. McCulloch, D. Bagnis, J. R. Durrant and J. Kim, *Adv. Energy Mater.*, 2019, **9**, 1803755.

16 J. Luke, E. J. Yang, C. Labanti, S. Y. Park and J.-S. Kim, *Nat. Rev. Mater.*, 2023, **8**, 839–852.

17 R. Sorrentino, E. Kozma, S. Luzzati and R. Po, *Energy Environ. Sci.*, 2021, **14**, 180–223.

18 Y. Yang, J. Wang, Y. Zu, Q. Liao, S. Zhang, Z. Zheng, B. Xu and J. Hou, *Joule*, 2023, **7**, 545–557.

19 P. Jiang, L. Hu, L. Sun, Z. Li, H. Han and Y. Zhou, *Chem. Sci.*, 2022, **13**, 4714–4739.

20 W. Lan, J. Gu, S. Wu, Y. Peng, M. Zhao, Y. Liao, T. Xu, B. Wei, L. Ding and F. Zhu, *EcoMat*, 2021, **3**(5), e12134.

21 K. W. Wong, H. L. Yip, Y. Luo, K. Y. Wong, W. M. Lau, K. H. Low, H. F. Chow, Z. Q. Gao, W. L. Yeung and C. C. Chang, *Appl. Phys. Lett.*, 2002, **80**, 2788–2790.

22 S. A. Salma, Q. A. Khoirun Nisa, R. F. Binti Nasrun, D. H. Son and J. H. Kim, *Mater. Today Energy*, 2023, **35**, 101297.

23 H. Bin, J. Wang, J. Li, M. M. Wienk and R. A. J. Janssen, *Adv. Mater.*, 2021, **33**, 2008429.

24 Y. Jiang, L. Sun, F. Jiang, C. Xie, L. Hu, X. Dong, F. Qin, T. Liu, L. Hu, X. Jiang and Y. Zhou, *Mater. Horiz.*, 2019, **6**, 1438–1443.

25 Y. Sun, C. J. Takacs, S. R. Cowan, J. H. Seo, X. Gong, A. Roy and A. J. Heeger, *Adv. Mater.*, 2011, **23**, 2226–2230.

26 Y. Lin, Y. Zhang, A. Magomedov, E. Gkogkosi, J. Zhang, X. Zheng, A. El-Labban, S. Barlow, V. Getautis, E. Wang, L. Tsetseris, S. R. Marder, I. McCulloch and T. D. Anthopoulos, *Mater. Horiz.*, 2023, **10**, 1292–1300.

27 H. Liu, Y. Xin, Z. Suo, L. Yang, Y. Zou, X. Cao, Z. Hu, B. Kan, X. Wan, Y. Liu and Y. Chen, *J. Am. Chem. Soc.*, 2024, **146**, 14287–14296.

28 H. Huang, G. Zhang, C. Xie, Z. Li, Q. Bai, B. He, M. Qiu, P. Han, H. Hu, S. Li and G. Zhang, *Adv. Funct. Mater.*, 2025, **35**, 2414844.

29 S. Gao, R. Peng, Y. Qiu, H. Liu, Y. Wu, X. Li, Y. Zhang, F. Jin and Z. Ge, *Adv. Funct. Mater.*, 2025, **35**, 2418223.

30 N. Zhang, W. Jiang, Y. An, Q. Liu, G. Du, T. Xia, D. Chen, C. Wong, X. C. Zeng, F. R. Lin, A. K. -Y. Jen and H. Yip, *Adv. Funct. Mater.*, 2025, 2423178.

31 J. Hu, C. He, X. Zheng, Y. Li, X. Yang, W. Wang, J. Zhang, Q. Chen, F. Huang, W. Fu and H. Chen, *Sol. RRL*, 2023, **7**, 2201106.

32 X. Sun, X. Ding, F. Wang, J. Lv, C. Gao, G. Zhang, X. Ouyang, G. Li and H. Hu, *ACS Energy Lett.*, 2024, **9**, 4209–4217.

33 K. G. Gebremariam, F. G. Hone, A. Negash, Z. Genene, J. Dai, A. G. Waketola, G. T. Mola, W. Mammo and N. A. Tegegne, *Energy Fuels*, 2024, **38**, 13304–13314.

34 X. Xiong, B. Hu, S. Tai, G. Lu, H. Fu and Q. Zheng, *Adv. Funct. Mater.*, 2025, 2505515.

35 G. Du, W. Jiang, N. Zhang, Y. Wang, M. Liu, T. Lei, Y. An, L. Ke, C. Ge, F. R. Lin, A. K.-Y. Jen and H.-L. Yip, *Energy Environ. Sci.*, 2025, **18**, 799–806.

36 S. Liu, J. Li, W. Xiao, R. Chen, Z. Sun, Y. Zhang, X. Lei, S. Hu, M. Kober-Czerny, J. Wang, F. Ren, Q. Zhou, H. Raza, Y. Gao, Y. Ji, S. Li, H. Li, L. Qiu, W. Huang, Y. Zhao, B. Xu, Z. Liu, H. J. Snaith, N.-G. Park and W. Chen, *Nature*, 2024, **632**, 536–542.

37 H. Xu, A. Sharma, J. Han, B. P. Kirk, A. R. Alghamdi, F. Xu, Y. Zhang, A. Emwas, G. Hizalan, S. De Wolf, M. R. Andersson, G. G. Andersson and D. Baran, *Adv. Energy Mater.*, 2024, **14**, 2401262.

38 W. T. Hadmojo, F. H. Isikgor, Y. Lin, Z. Ling, Q. He, H. Faber, E. Yengel, R. Ali, A. Samad, R. E. A. Ardhi, S. Y. Jeong, H. Y. Woo, U. Schwingenschlögl, M. Heeney and T. D. Anthopoulos, *Energy Environ. Mater.*, 2024, **7**, e12712.

39 F. Liu, S. Shao, X. Guo, Y. Zhao and Z. Xie, *Sol. Energy Mater. Sol. Cells*, 2010, **94**, 842–845.

40 Y. Lin, Y. Firdaus, F. H. Isikgor, M. I. Nugraha, E. Yengel, G. T. Harrison, R. Hallani, A. El-Labban, H. Faber, C. Ma, X. Zheng, A. Subbiah, C. T. Howells, O. M. Bakr, I. McCulloch, S. De Wolf, L. Tsetseris and T. D. Anthopoulos, *ACS Energy Lett.*, 2020, **5**, 2935–2944.

41 J.-G. Choi and L. T. Thompson, *Appl. Surf. Sci.*, 1996, **93**, 143–149.

42 Y. Sun, C. J. Takacs, S. R. Cowan, J. H. Seo, X. Gong, A. Roy and A. J. Heeger, *Adv. Mater.*, 2011, **23**, 2226–2230.

43 B. C. O'Regan, K. Bakker, J. Kroeze, H. Smit, P. Sommeling and J. R. Durrant, *J. Phys. Chem. B*, 2006, **110**, 17155–17160.

44 F. H. Isikgor, S. Zhumagali, L. V. T. Merino, M. De Bastiani, I. McCulloch and S. De Wolf, *Nat. Rev. Mater.*, 2022, **8**, 89–108.

45 C. Chen, L. Wang, W. Xia, K. Qiu, C. Guo, Z. Gan, J. Zhou, Y. Sun, D. Liu, W. Li and T. Wang, *Nat. Commun.*, 2024, **15**, 6865.

46 C. Liu, Y. Fu, J. Zhou, L. Wang, C. Guo, J. Cheng, W. Sun, C. Chen, J. Zhou, D. Liu, W. Li and T. Wang, *Adv. Mater.*, 2024, **36**, 2308608.

47 D. Li, L. Wang, C. Guo, Y. Liu, B. Zhou, Y. Fu, J. Zhou, D. Liu, W. Li and T. Wang, *ACS Mater. Lett.*, 2023, **5**, 2065–2073.

48 Y. Lin, Y. Firdaus, F. H. Isikgor, M. I. Nugraha, E. Yengel, G. T. Harrison, R. Hallani, A. El-Labban, H. Faber, C. Ma, X. Zheng, A. Subbiah, C. T. Howells, O. M. Bakr, I. McCulloch, S. De Wolf, L. Tsetseris and T. D. Anthopoulos, *ACS Energy Lett.*, 2020, **5**, 2935–2944.

49 B. Xiao, M. Zhang, J. Yan, G. Luo, K. Gao, J. Liu, Q. You, H.-B. Wang, C. Gao, B. Zhao, X. Zhao, H. Wu and F. Liu, *Nano Energy*, 2017, **39**, 478–488.

50 T. M. Clarke, C. Lungenschmied, J. Peet, N. Drolet and A. J. Mozer, *Adv. Energy Mater.*, 2015, **5**, 1401345.

51 J. Gao, X. Ma, C. Xu, X. Wang, J. H. Son, S. Y. Jeong, Y. Zhang, C. Zhang, K. Wang, L. Niu, J. Zhang, H. Y. Woo, J. Zhang and F. Zhang, *Chem. Eng. J.*, 2022, **428**, 129276.